Progress In Electromagnetics Research M, Vol. 133, 11–19, 2025

PIER M

(Received 15 February 2025, Accepted 12 March 2025, Scheduled 20 March 2025)

Optimizing Radar Stealth by Near-Field Diagnostics of Aircraft Engine Absorbent Material Coating

Yulang Li[1, 2, 3], Hongwei Deng[4, 5], Linyuan Dou[1, 2, 3], and Zeyong Wei[1, 2, 3, *]

[1] *School of Physics Science and Engineering, Tongji University, Shanghai 200092, China*
[2] *Institute of Precision Optical Engineering, Tongji University, Shanghai 200092, China*
[3] *MOE Key Laboratory of Advanced Micro-Structured Materials, Shanghai 200092, China*
[4] *School of Power and Energy, Northwestern Polytechnical University, Xian 710072, China*
[5] *AECC Shenyang Engine Research Institute, Shenyang 110015, China*

ABSTRACT: This study introduces an approach for applying radar absorbing material (RAM) coatings on aircraft engines to reduce monostatic radar cross-section (mono RCS), leveraging near-field diagnostic analysis to guide the process. The primary goal is to improve the mono RCS stealth performance within the engine's intricate cavity structure. The finite-difference time-domain (FDTD) method is employed to accurately compute near-field distributions within the cavity, accounting for the complex interactions of electromagnetic wave propagation and scattering. This analysis method identifies critical hot spots within the engine cavity that significantly impact the RCS. An RAM coating scheme is then designed to target these "hot spots", resulting in substantial RCS reduction of the engine. The findings highlight the accuracy and effectiveness of this methodology, offering valuable contributions to the advancement of stealth technologies for next-generation aircraft engines.

1. INTRODUCTION

The aircraft engine is classified as an electrically large cavity structure and exhibits a high monostatic radar cross section (mono RCS) [1–5]. RCS reduction approaches for the engine employ two principal approaches: geometry optimization and the utilization of radar absorbing materials (RAM) [6–9]. Geometry optimization typically involves a comprehensive optimization of the geometrical parameters of critical engine components — such as the nozzle, center cone, scroll blade, and flame stabilizer [7, 10–12] while high-frequency computational techniques, including Shooting and Boundary Ray (SBR) and Iterative Physical Optics (IPO) algorithms, are utilized to rapidly compute the RCS [13, 14]. These methods are commonly coupled with deep learning to enhance the efficacy of mono RCS reduction [15, 16]. The engine's geometrical design parameters, including various aspect ratios and the contour of the engine exhaust pipe, are optimized to determine the most effective configuration for enhancing the RCS stealth characteristics of the aircraft engine [8, 12, 15–21].

RAM is a kind of special material that can absorb rather than reflect radar waves and achieves concealment effect by reducing the intensity of radar echo of the target object. Tailoring the application of RAM requires consideration of both the intrinsic absorption properties of the materials and their strategic placement within the engine cavity [1, 6, 22–24]. Although materials with broad bandwidth and high absorptivity are preferred, their specific application or coating scheme can significantly influence the overall RCS stealth optimization outcomes. Moreover, the complex electromagnetic coupling phenomena inherent in the aircraft engine complicate the identification of an optimal coating scheme for RAM through simplistic approaches, thereby restricting enhancements in RCS stealth performance [2–4, 14, 25, 26]. Traditional diagnostic methodologies based on ISAR imaging — which conceptualize the scattering distribution of a target as a series of discrete isolated scattering centers — are applicable to simple geometric design but fall short in elucidating the complex resonant scattering mechanisms within the engine cavity, thereby impeding the development of effective stealth diagnostics [27–29]. In the current study, near-field analysis techniques have demonstrated their efficacy in facilitating engine stealth optimization [15, 30], with RCS reduction achievable through the mitigation of "hot spots" in the field distribution.

In this study, we propose a method based on near-field diagnostics that leverages the Finite-Difference Time-Domain (FDTD) method to rapidly ascertain the propagation characteristics of electromagnetic waves within the aircraft engine [31]. This approach enables the identification of electromagnetic wave transmission "hot spots" within the engine cavity. By exploiting these identified hot spot locations, a suitable coating scheme employing wave-absorbing materials is implemented to optimize the overall RCS stealth performance of the engine.

The structure of this work is organized as follows. In Section 3, we initially calculate the near-field distribution within a simple cavity featuring an internal convex structure, subsequently applying radar-absorbing material to the identified hot spots. The results are then compared with those obtained from coating schemes applied to non-hot spot regions, thereby validating the feasibility of the proposed methodology. Section 4

---

* Corresponding author: Zeyong Wei (weizeyong@tongji.edu.cn).

doi:10.2528/PIERM25021503

Published by THE ELECTROMAGNETIC ACADEMY

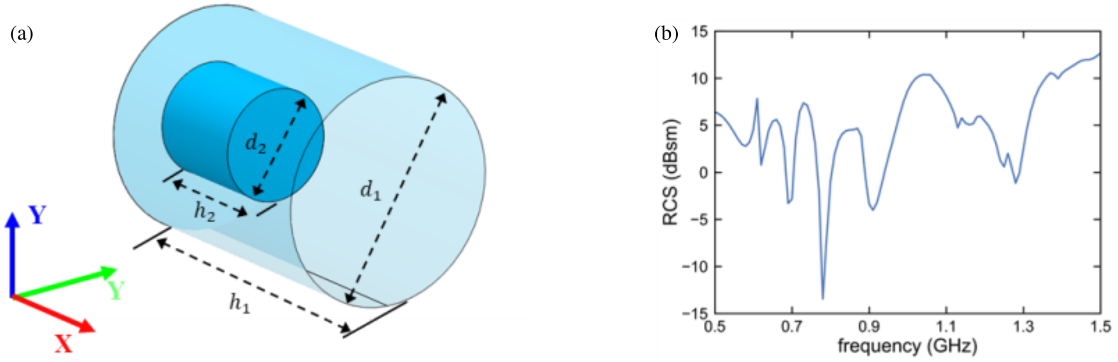

FIGURE 1. (a) Simplified geometric structure of the model and h_1 and d_1 are the height and diameter of the outer cylinder, and h_2 and d_2 are the height and diameter of the inner cylinder, respectively; (b) The mono RCS (HH) of the simplified model of 0.5 to 1.5 GHz electromagnetic wave incidence under the condition of $\theta = 0^\circ$ and $\varphi = 0^\circ$.

focuses on an actual engine model, where the near-field distribution is computed, and various coating schemes are devised based on the identified hot spots within the engine's field distribution, underscoring the merits of radar stealth optimization approaches grounded in near-field diagnostics.

2. SIMPLIFIED MODEL

We analyze a simplified engine cavity model whose geometric structure is illustrated in Figure 1(a). The model comprises an outer cylindrical shell with a height of $h_1 = 800\,\text{mm}$ and a diameter of $d_1 = 600\,\text{mm}$, as well as an inner cylinder with a height of $h_2 = 300\,\text{mm}$ and a diameter of $d_2 = 150\,\text{mm}$. The cavity opening is oriented along the positive x-axis. To further simplify the model, we employ a closed terminal at the other end of the engine opening; the error between the closed terminal and the open terminal is deemed acceptable for simulation calculations [25].

This work focuses on optimizing the mono RCS for varying elevation angles at the cavity's resonant frequency. To ensure an accurate characterization of the cavity's electromagnetic response, the FDTD method is employed to compute the mono RCS for both the simplified cavity model and a real engine geometry. This approach guarantees the reliability of the cavity's RCS calculations. We use the FDTD solver toolkit in our self-developed software called WGallop as the mono RCS solver. In the FDTD simulation, the Yee cell grid size is set to 1/20 of the wavelength; the maximum number of iterations is 20000; each iteration lasts 0.0016 ns; and the convergence error threshold is 35 dB. These settings ensure accuracy and stability.

Figure 1(b) illustrates the simulation results of the mono RCS for the simplified cavity model across an incident frequency range of 0.5–1.5 GHz. Within this spectrum, a pronounced resonance phenomenon is observed at 1 GHz, where the mono RCS of the simplified cavity exhibits a significant enhancement compared to other frequencies. Both the incidence polarization mode and acceptance polarization mode are horizontal polarization, as the simplified model maintains consistency for the mono RCS between horizontally polarized incidence and vertically polarized reflection.

The incident plane wave used in the simulation has a field intensity of 1 V/m. To leverage this resonance effect, we have concentrated on optimizing the application of RAM coatings specifically at this resonant frequency. This approach aims to achieve a more pronounced contrast effect, which is critical for enhancing stealth performance across various angles of incidence at the 1 GHz resonant frequency. The computational results of this optimization are presented graphically in Figure 2.

Figure 2(a) presents the simulation results for the mono RCS of the simplified model under horizontally polarized incidence across varying elevation angles (θ ranging from 0 to 60°), with the azimuth angle fixed at $\varphi = 0^\circ$. The resonance angle in this configuration is identified as $\theta = 26^\circ$, which refers to the angle at which the mono RCS exhibits an oscillation peak as it varies with the angle of incidence. Figures 2(b) and 2(c) provide detailed visualizations of the electric and magnetic field distributions within the simplified model at the resonance angle of $\theta = 26^\circ$.

The results reveal that, under horizontal polarization, the most intense electric field is confined to the outer region of the model, unable to enter the deep cavity. This phenomenon is likely attributed to the resonance mode characteristics of the simplified geometry, which primarily enhance the field near the opening. In contrast, the magnetic field exhibits peak intensity along the edges of the inner cylindrical structure, likely due to geometric discontinuities that enhance local magnetic field intensity.

Figure 2(d) presents the simulation results for the mono RCS of the simplified model under vertically polarized incidence across varying elevation angles (θ ranging from 0 to 60°). The resonance angle in this scenario is predominantly identified as $\theta = 31^\circ$, based on the peak RCS observed in the simulation results. Figures 2(e) and 2(f) provide detailed visualizations of the electromagnetic field distribution in the xOz-plane within the cavity of the engine model at the resonance angle.

The results demonstrate that electromagnetic waves propagate deeply into the cavity of the simplified model, leading to a significant resonance phenomenon. A hot spot in the field distribution is notably formed at the cavity termination. In contrast to horizontal polarization, where hot spots are concentrated in

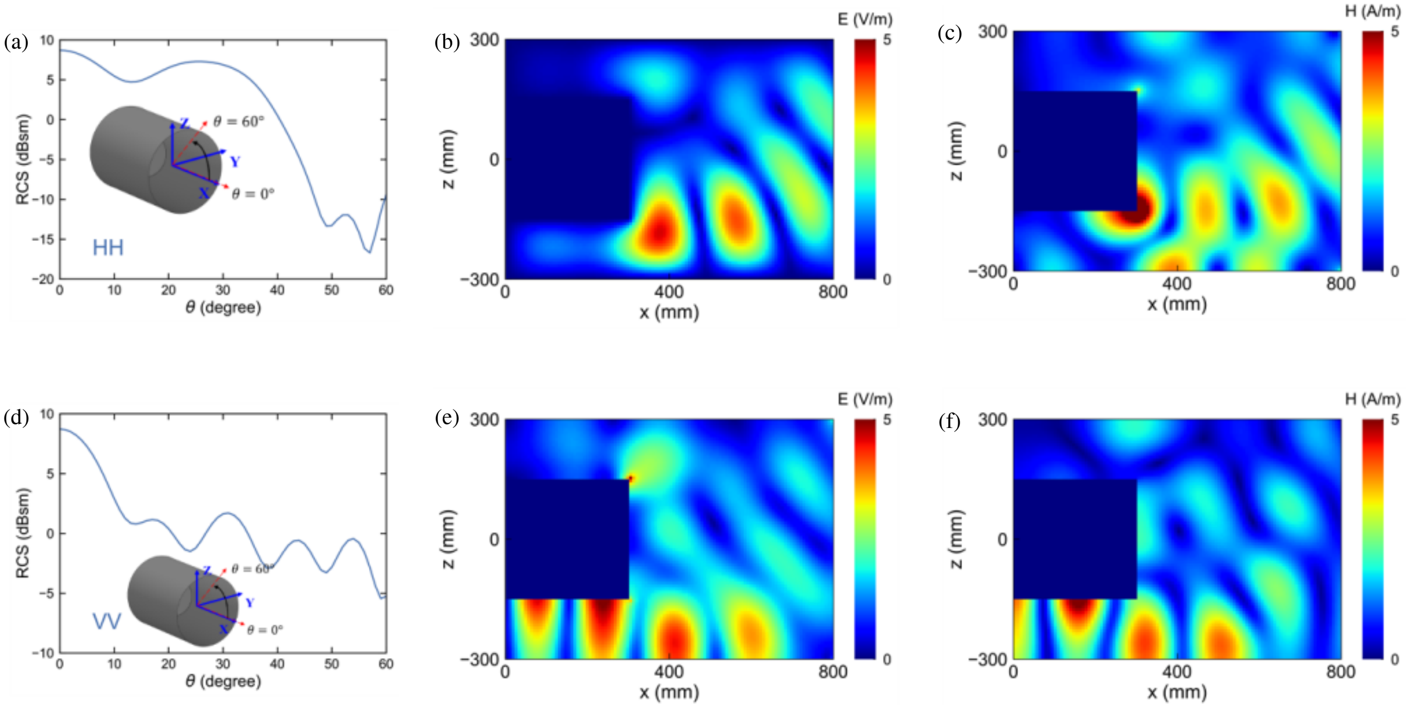

FIGURE 2. (a) Mono RCS (HH) elevation angular distribution at 1 GHz; (b) Electric field distribution inside the engine with horizontally polarization incident at $\theta = 26°$; (c) Magnetic field distribution inside the engine with horizontally polarization incident at $\theta = 26°$; (d) Mono RCS(VV) elevation angular distribution at 1 GHz; (e) Electric field distribution inside the engine with vertical polarization polarized incident at $\theta = 31°$; (f) Magnetic field distribution inside the engine with vertical polarization incident at $\theta = 31°$.

the outer region, vertical polarization produces hot spots along the inner surface of the cavity. This distribution is more favorable for the application of RAM, as the concentrated field provides a focused region for efficient material absorption.

Given the more useful field distribution observed in vertical polarization than horizontal polarization, our subsequent discussions and analyses will primarily focus on the vertical polarization scenario, which offers greater potential for achieving optimal stealth performance through targeted material application.

For actual calculations, these parameters are fitted using the Debye model to ensure compatibility with the FDTD algorithm. In this work, the RAM employed is exclusively this material. Based on the data provided in Table 1 by the AECC Shenyang Engine Research Institute, we use the Debye model described by Equations (1) and (2) for parameter fitting, with the corresponding parameter values listed as follows: $\varepsilon_\infty = 24.8447$; $\varepsilon_s = 34.2461$; $\tau_\varepsilon = 2.61 \times 10^{-11}$ s; $\mu_\infty = 0.383913$; $\mu_s = 2.86361$; $\tau_\mu = 3.19 \times 10^{-11}$ s. The ε and μ of the RAM at different frequencies are shown in Table 1.

$$\varepsilon_r = \varepsilon_\infty + \frac{\varepsilon_s - \varepsilon_\infty}{1 + j\omega\tau_\varepsilon} \tag{1}$$

$$\mu_r = \mu_\infty + \frac{\mu_s - \mu_\infty}{1 + j\omega\tau_\mu} \tag{2}$$

Figure 3(a) illustrates the coating scheme for RAM applied to the interior cavity wall of the simplified model. In this scheme, a ring-shaped coating with a length of 300 mm and a material thickness of 3 mm is implemented. This approach differs from a hot spot-specific strategy by uniformly distributing the RAM along the internal cavity surface rather than concentrating it directly on the hot spots.

TABLE 1. Dielectric constant and permeability of RAM at different frequencies.

f/GHz	ε_{real}	ε_{imag}	μ_{real}	μ_{imag}
2	33.332994	2.78401	2.5203037	0.85640901
3	32.414035	3.7239114	2.205127	1.0950975
4	31.417775	4.3117041	1.8933664	1.2101808
5	30.466446	4.6095829	1.6210764	1.2398456
6	29.621467	4.7000845	1.3975854	1.2190442
7	28.900941	4.6563133	1.2192475	1.1720037
8	28.299626	4.5326183	1.0782896	1.1134113
9	27.802659	4.3657111	0.9668137	1.051496
10	27.392982	4.1789564	0.87813614	0.99058928
11	27.054681	3.9865898	0.8069966	0.93280191
12	26.77414	3.7969328	0.74938034	0.87902325
13	26.540194	3.6145978	0.70225778	0.82949093
14	26.343876	3.4419213	0.66334596	0.78410859
15	26.178053	3.2798712	0.63091772	0.74262072
16	26.03707	3.1286103	0.60365761	0.70470728
17	25.916438	2.987845	0.58055548	0.67003395
18	25.812583	2.8570368	0.56082878	0.63827763

Figure 3(b) presents an optimized coating scheme tailored to the electric and magnetic field distribution hot spots observed in the simplified model. In this configuration, RAM is applied

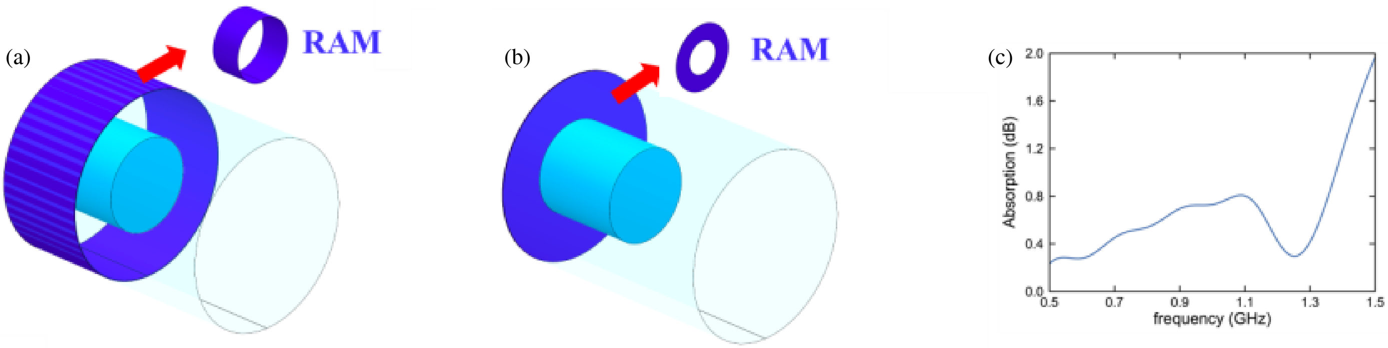

FIGURE 3. (a) The cavity internal surface coating scheme; (b) The cavity termination coating scheme; (c) The specific absorption rate of the metallic mono RCS for an absorbing material with a coating thickness of $d = 3$ mm across frequencies from 0.5 to 1.5 GHz.

selectively at the cavity terminus corresponding to the identified hot spots, with a material thickness of 3 mm. Figure 3(c) depicts the wave-absorbing properties of the coated materials at 1–1.5 GHz.

Figure 4 presents the simulation results for the mono RCS of the simplified model, evaluating the performance of various RAM coating schemes. In the absence of any RAM coating, the mono RCS at an incidence angle of $\theta = 31°$ is measured at 1.21 dBsm. When the cavity's internal surface is uniformly coated with absorbing material, the mono RCS at $\theta = 31°$ increases to 3.81 dBsm, representing an increase exceeding 2 dB relative to the uncoated case. In contrast, the cavity termination coating scheme produces a mono RCS of -6.00 dBsm at the same angle, corresponding to a reduction of more than 7 dB compared to the uncoated result. Furthermore, within the incidence angle range from 0 to 60°, this targeted coating approach reduces the mono RCS by 5.61 dB, markedly outperforming the uniform coating scheme. This enhanced performance is attributed to the precise alignment of the RAM placement with the near-field distribution hot spots, as identified in Figures 2(e) and 2(f). By applying RAM to the regions exhibiting the highest field intensity and effectively mitigating the resonance phenomenon, the cavity termination coating scheme optimizes the mono RCS of the simplified model. This approach clearly demonstrates the critical role of detailed field distribution analysis in designing advanced stealth coatings.

Figure 5 presents the internal electric and magnetic field distributions of the simplified model under various RAM coating schemes, analyzed under the resonance condition ($\theta = 31°$). Figure 5(a) and Figure 5(b) show that the uniform coating applied to the entire internal cavity surface produces minimal changes in the near-field hot spots. As a result, the mono RCS remains nearly unchanged, which is confirmed by the simulation results in Figure 4.

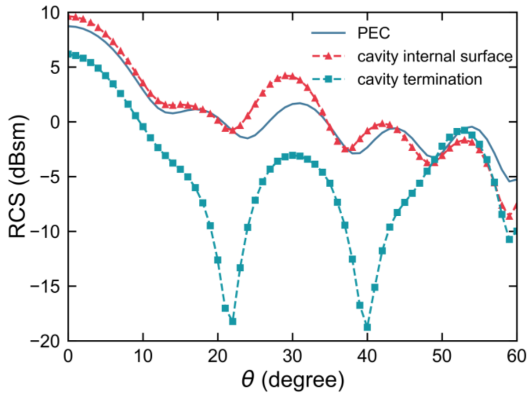

FIGURE 4. Mono RCS (VV) simulation result for a simplified model, subjected to an incident frequency of 1 GHz. Results are presented for two stealth optimization schemes: the default RAM coating and a coating scheme designed based on field distribution hot spots.

In contrast, Figure 5(c) and Figure 5(d) illustrate the effect of the cavity termination coating scheme. The results indicate that the hot spot at the bottom of the cavity contributes minimally to the mono RCS, whereas hot spots closer to the cavity opening have a more significant impact on the mono RCS. This observation is consistent with the results for vertical polarization incidence in the simplified model (see Figures 2(b) and 2(c)), where larger RCS values are associated with hot spots that are concentrated toward the exterior of the cavity. Additionally, the uniform coating scheme does not sufficiently weaken the hot spots in the forward part of the cavity, resulting in less effective RCS reduction at certain incidence angles. In contrast, the targeted cavity termination coating scheme significantly modifies the near-field distribution by reducing the overall electric field magnitude and shifting the magnetic field hot spot from the cylindrical surface to the bottom of the cavity. These modifications directly contribute to the substantial mono RCS reduction observed with this scheme, as demonstrated in Figure 4.

Using near-field diagnostics, we identified the critical hot spots within the cavity of the simplified model and designed a RAM coating scheme specifically targeted at these regions. A comparative analysis with other coating approaches confirms the superior performance of the hot spot-targeted design, thereby validating the feasibility of an optimization method based on near-field diagnostic coating approaches.

3. REAL ENGINE MODEL

Figure 6 illustrates the real aircraft engine model from different perspectives. Figure 6(a) shows a view in the xOz-plane, while Figure 6(b) presents the view in the yOz-plane. The engine model has the following dimensions: length $l = 1$ m, width

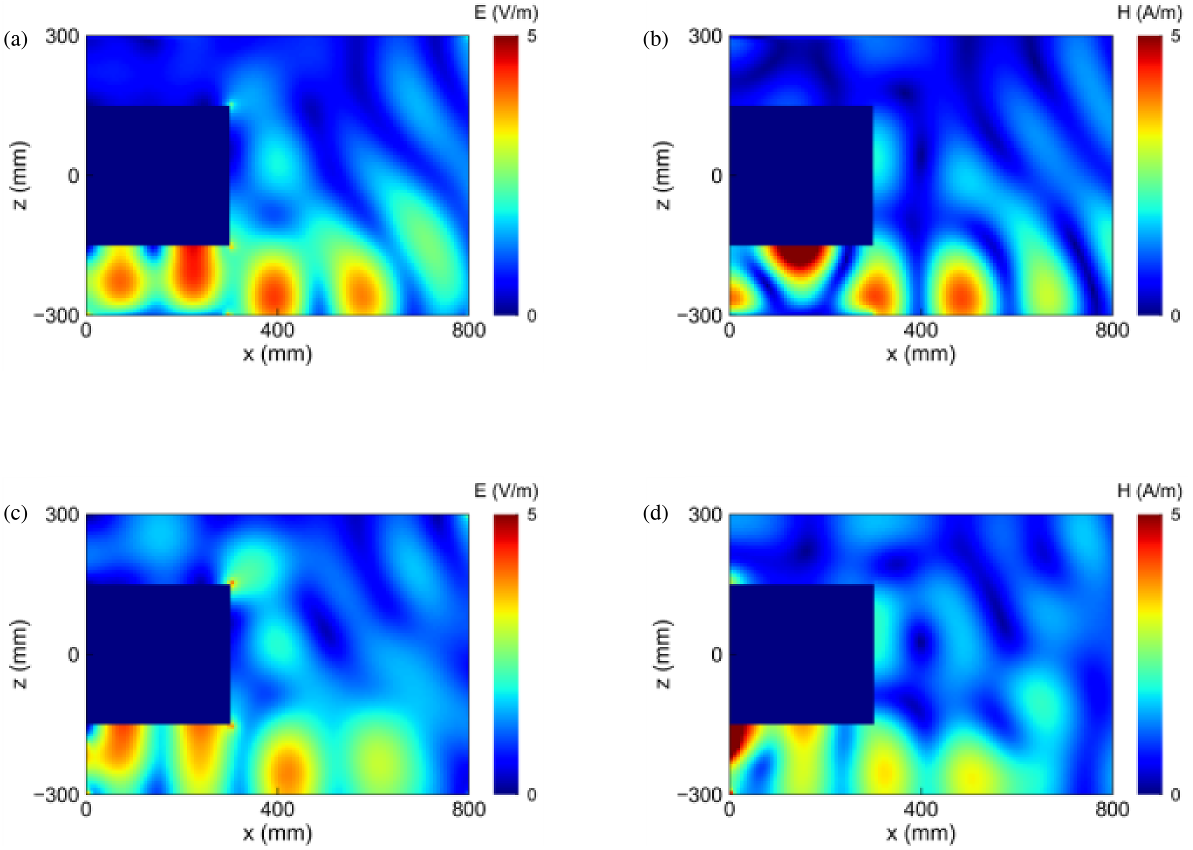

FIGURE 5. (a) Electric field distribution with cavity internal surface coating scheme; (b) Magnetic field distribution with cavity internal surface coating scheme; (c) Electric field distribution with cavity termination coating scheme; (d) Magnetic field distribution with cavity termination coating scheme.

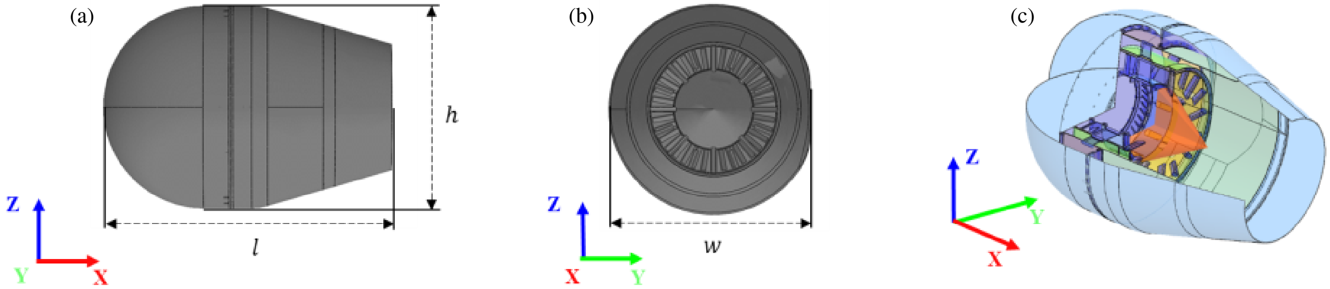

FIGURE 6. (a) Engine model xOz-plane view, where l and h are the length and height of the engine; (b) Engine model yOz-plane view and w is the width of the engine; (c) Schematic diagram of engine internal structure.

$w = 0.7$ m, and height $h = 1$ m. Figure 6(c) provides a three-dimensional representation of the engine structure, incorporating key components such as the center cone, bearing support, turbine blades, mixer barrel, flame stabilizer, afterburner, and symmetrical nozzles.

Figure 7(a) presents the simulation results for the mono RCS of the engine model at incident frequencies of 3, 6, and 10 GHz. The simulations were conducted under vertical polarization, with an azimuth angle of $\varphi = 0°$ and elevation angles varying from $\theta = 0$ to 60°. The results indicate that the engine cavity's RCS is most significantly influenced at an incident frequency of 10 GHz. As the incidence angle varies, several RCS peaks emerge, with the highest value approaching 15 dBsm. To facilitate a clear comparison following the application of the RAM coating, the optimization of the RAM coating scheme was based on the 10 GHz simulation results. In these simulations, the incident wave amplitude was set to 1 V/m. Detailed analysis reveals pronounced mono RCS peaks at elevation angles of 2°, 6°, 16°, and 28°, which are likely attributable to engine cavity resonance or edge diffraction and are accompanied by the development of distinct field distribution hot spots within the engine. Figure 7(b) shows the comparison results between the experimental test mono RCS provided by the AECC Shenyang Engine Research Institute and the simulation mono

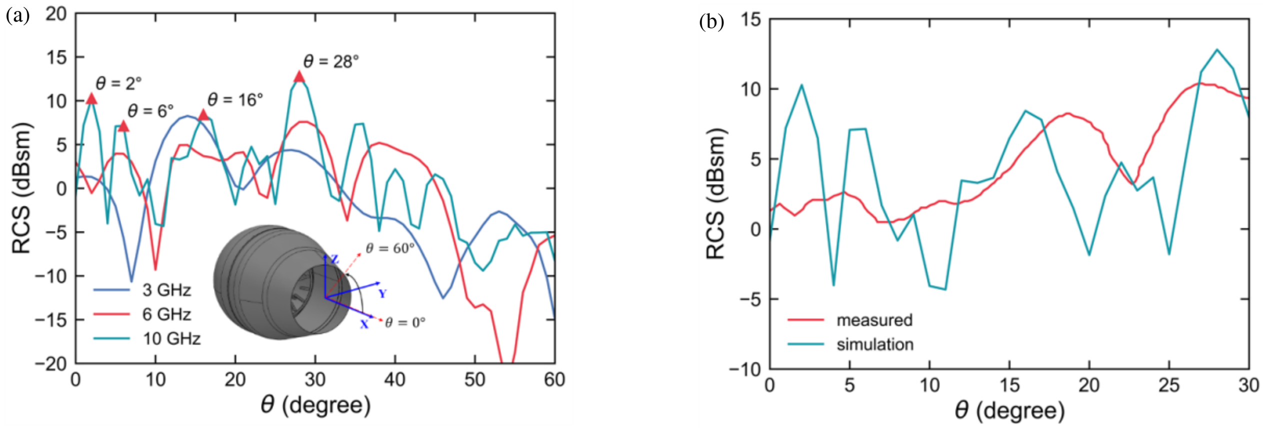

FIGURE 7. (a) Simulation results of monostatic RCS of the engine model at different incidence frequencies. Angles $\theta = 2^\circ, 6^\circ, 16^\circ$, and 28° indicate the resonance effects of the engine cavity on incident electromagnetic waves;(b) The simulation results and the measured results at 10 GHz.

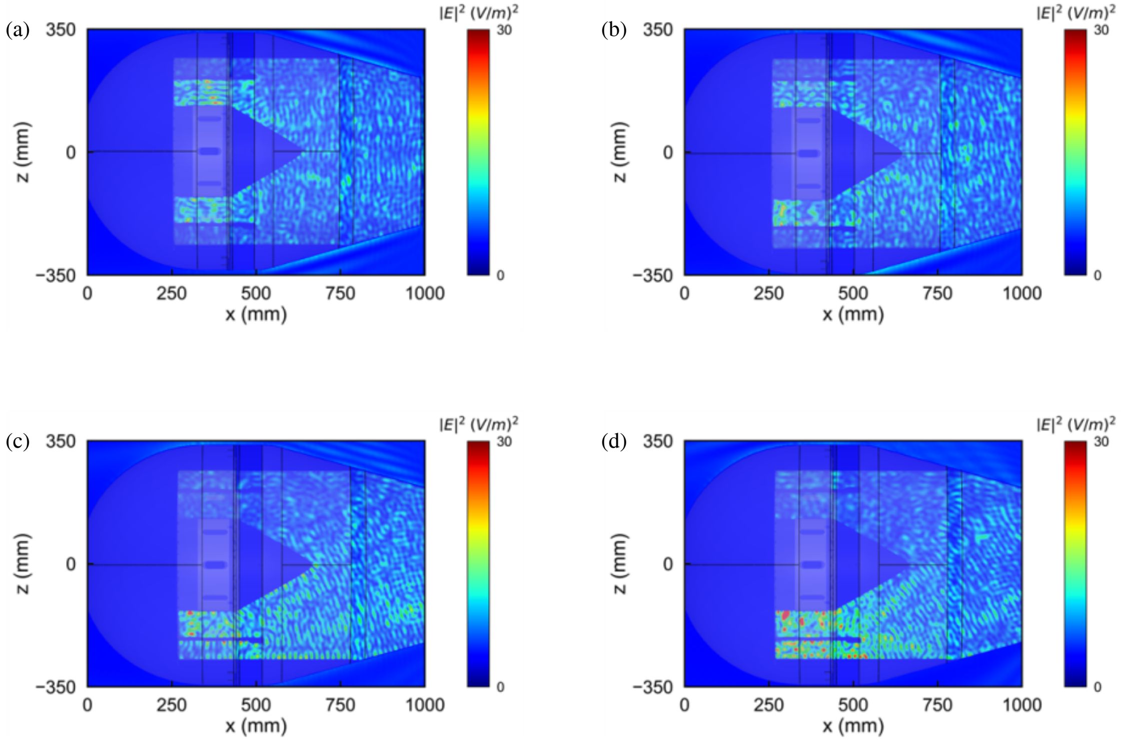

FIGURE 8. Incident frequency at 10 GHz with vertical polarization: Internal electric field distribution within the engine model at various elevation angles: (a) Elevation angle $\theta = 2^\circ$; (b) Elevation angle $\theta = 6^\circ$; (c) Elevation angle $\theta = 16^\circ$; (d) Elevation angle $\theta = 28^\circ$.

RCS of the engine cavity. It can be seen that the actual resonance angles around 16° and 28° are in good agreement with the experiment.

To address real model mono RCS reduction, we conducted a detailed analysis of the internal resonant modes at these four critical angles and developed corresponding RAM coating schemes. These schemes are designed to mitigate the effects of cavity resonance by strategically optimizing the placement and properties of the absorbing material. By targeting these critical resonance angles, the coatings effectively suppress the radar signatures, leading to a substantial reduction in the overall mono RCS of the engine and an enhancement in its stealth performance. To emphasize the distribution of hot spots, the square of the electric field (in $\mathrm{V}^2/\mathrm{m}^2$) is used as the unit of measurement.

The electric field distributions within the engine model at four distinct resonance angles are presented in Figure 8. Figure 8(a) shows the distribution at an elevation angle of $\theta = 2^\circ$, where the incident wave is nearly perpendicular to the surface. At this angle, the electric field hot spots are primarily concentrated on the surface of the central cone within the cavity, and the field intensity gradually decreases as the distance from the cavity opening increases. Electromagnetic waves are largely obstructed from penetrating deeper into the cavity, with the

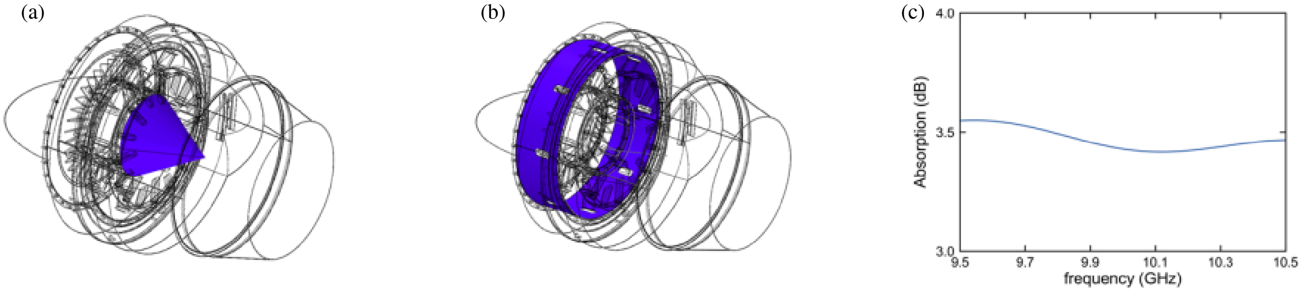

FIGURE 9. (a) Uniform RAM coating applied to the central cone surface; (b) Targeted RAM coating applied to the bearing support at the engine's rear end; (c) Absorption efficiency of mono RCS with a 3 mm RAM thickness across 9.5–10.5 GHz.

maximum squared electric field intensity ($|E|^2$) reaching approximately 20 $\mathrm{V}^2/\mathrm{m}^2$.

Figure 8(b) illustrates the distribution at an elevation angle of $\theta = 6^\circ$. Here, the electric field hot spots gradually shift from the surface of the central cone toward the bypass duct. Although the field intensity in the upper regions of the cavity decreases significantly, the maximum intensity along the surface of the central cone remains around 20 $\mathrm{V}^2/\mathrm{m}^2$. Figure 8(c) displays the distribution at an elevation angle of $\theta = 16^\circ$. At this angle, the electric field on the surface of the central cone is markedly diminished, and the predominant hot spots relocate entirely to the bypass duct. While the overall electric field magnitude is similar to that at $\theta = 2^\circ$ and $\theta = 6^\circ$, some localized regions exhibit higher intensities, with $|E|^2$ peaking at approximately 30 $\mathrm{V}^2/\mathrm{m}^2$.

At an elevation angle of $\theta = 28^\circ$, as shown in Figure 8(d), the electric field is distinctly concentrated within the bypass duct, resulting in a much higher intensity than the lower angles, with the maximum $|E|^2$ exceeding 30 $\mathrm{V}^2/\mathrm{m}^2$. This notable increase indicates that resonance at $\theta = 28^\circ$ is the most pronounced among the four angles analyzed.

Based on the location of the field distribution hot spots and the maximum field intensities, the RAM coating scheme is specifically tailored to address the conditions at $\theta = 28^\circ$, where both resonance and field intensity reach their peak. This targeted approach ensures that the mitigation measures are optimized to effectively suppress the mono RCS at this critical angle.

Figure 9 compares the RAM coating schemes for the aircraft engine. In Figure 9(a), the first coating scheme is illustrated, where the RAM is uniformly applied to the central cone surface within the engine cavity. This conventional method does not account for the spatial variation of the electric field distribution, which limits its effectiveness in reducing the mono RCS. In contrast, the second coating scheme, depicted in Figure 9(b), strategically applies the RAM to the bearing support at the rear end of the engine. This targeted placement is based on electric field distribution analysis, which identifies the bearing support as a critical area for mono RCS reduction.

Figure 9(c) displays the absorption efficiency of the mono RCS for both coating methods with a 3 mm RAM thickness over a frequency range of 9.5 GHz to 10.5 GHz. We aim to highlight the advantages of designing RAM coating schemes based on the field distribution hot spots within the engine cavity by employing two entirely different design approaches.

Figure 10 presents the simulation results for the mono RCS of the engine model under different RAM coating schemes. The figure compares the mono RCS over the elevation angle range of 0–60° at an incident frequency of 10 GHz with vertical polarization and an azimuth angle of $\varphi = 0^\circ$. When the RAM coating is uniformly applied to the central cone (as shown in Figure 9(a)), the average mono RCS decreases by 7.52 dB for elevation angles between 45° and 60°, while the average reduction within the 0°–60° range is 2.90 dB. However, this uniform scheme does not suppress resonance effects at the critical angles ($\theta = 2^\circ$, 6°, 16°, and 28°), where pronounced RCS peaks remain. As shown in Figure 11(a), applying RAM in areas without significant electric field hot spots fails to weaken the hot spots in the engine passage, as they remain similar to those of the uncoated condition, thus impeding a substantial reduction in the aircraft engine's RCS.

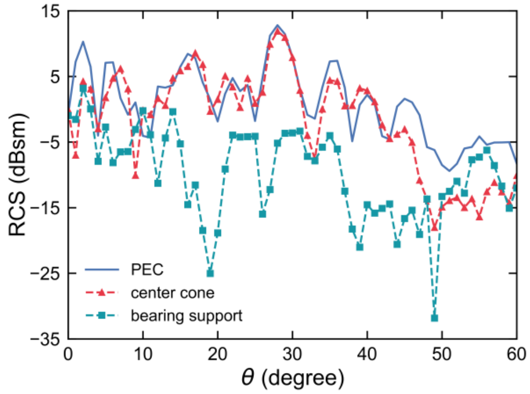

FIGURE 10. Mono RCS simulation results for RAM coating schemes ($\theta = 0$ to 60°).

In contrast, the RAM coating scheme targeted at the bearing support (Figure 9(b)) demonstrates significantly improved performance. For elevation angles between 0° and 45°, the mono RCS is reduced by 12 dB. At resonance angles, the reductions are dramatic: at $\theta = 2^\circ$, the mono RCS drops from 10.28 dBsm to 3.19 dBsm; at $\theta = 6^\circ$, it decreases from 7.14 dBsm to -8.14 dBsm; at $\theta = 16^\circ$, it falls from 8.14 dBsm to -14.55 dBsm; and at $\theta = 28^\circ$, it decreases from 12.80 dBsm

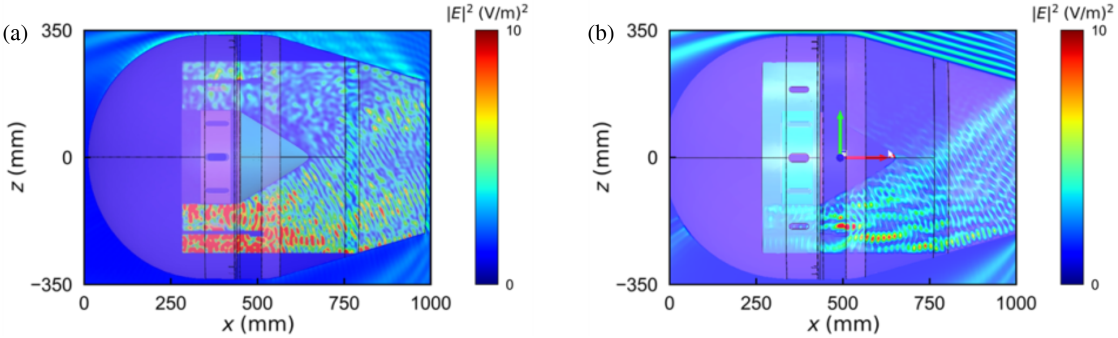

FIGURE 11. (a) Internal electric field distribution with RAM coating applied to the central cone; (b) Internal electric field distribution with RAM coating applied to the bearing support.

to -5.41 dBsm. For elevation angles between 45° and 60°, the average mono RCS is reduced by 8 dB. When the RAM is applied to the bearing support at the engine's rear end, it is deposited on the interior of the support frame based on the hot spots observed in the field distribution shown in Figure 11(b). This targeted application effectively eliminates the hot spot within the engine chamber. Compared with the uncoated case (Figure 8(d)), the hot spots on the bypass are nearly eliminated, thereby achieving effective RCS reduction.

By designing RAM coating schemes informed by field distribution analysis, this study demonstrates the effectiveness of aligning material placement with field intensity hot spots. The hot spot-targeted coating significantly suppresses resonance-related scattering sources, reduces mono RCS at critical angles, and achieves comprehensive stealth optimization across a wide range of incidence angles.

4. CONCLUSION

In this study, we investigate the feasibility of reduction the mono RCS via near-field diagnostic techniques. Our approach begins with a detailed analysis of a simplified cavity model to identify the incident angles that most significantly impact the mono RCS, as evidenced by simulation data. We then examine the corresponding field distributions at these critical angles and refine the application of RAM within the cavity accordingly. The effectiveness of this strategy is validated through an evaluation of the near-field hot spot distribution patterns.

Subsequently, the methodology is extended to an actual aircraft engine model. By computing the mono RCS across a broad range of elevation angles, we identify the resonant angles that exert the greatest influence. Detailed field distribution analyses at these angles guide the optimized placement of RAM within the engine, thereby effectively mitigating hot spots and significantly reducing the engine's mono RCS.

Collectively, these two case studies underscore the pivotal role of near-field diagnostics in RCS optimization. This approach not only enhances the performance of RAM coatings but also highlights the indispensable importance of detailed field analysis in designing effective stealth measures. The findings affirm the efficacy of near-field analysis as a robust tool for RCS reduction, offering valuable insights for the advancement of stealth technologies and radar engineering applications.

ACKNOWLEDGEMENT

This study was supported by the National Key R&D Plan of China (Grant No.2022YFF0604802) and Shanghai Municipal Science and Technology Major Project; School of Power and Energy (Northwestern Polytechnical University, Xian 710072, China); AECC Shenyang Engine Research Institute (Shenyang, 110015, China).

REFERENCES

[1] Kim, Y.-D., H. Lim, J.-H. Han, W.-Y. Song, and N.-H. Myung, "RCS reduction of open-ended circular waveguide cavity with corrugations using mode matching and scattering matrix analysis," *Progress In Electromagnetics Research*, Vol. 146, 57–69, 2014.

[2] Noh, Y.-H., C.-S. Park, J.-G. Yook, W.-Y. Choi, and Y.-H. Jang, "Analysis for contribution of engine inlet structure to monostatic RCS of aircraft in the VHF band," in *2018 IEEE International Symposium on Antennas and Propagation & USNC/URSI National Radio Science Meeting*, 2335–2336, Boston, MA, USA, Jul. 2018.

[3] Chung, S. S. M. and S.-C. Tuan, "Shadowing a small size but large radar cross section object with a large size but small radar cross section object," in *2020 IEEE Asia-Pacific Microwave Conference (APMC)*, 1051–1053, Hong Kong, Dec. 2020.

[4] Zohuri, B., *Radar Energy Warfare and the Challenges of Stealth Technology*, Springer, 2020.

[5] Grant, R., "The radar game," Mitchell Institute, 2010.

[6] Lee, C., S. Lee, and R. Chou, "RCS reduction of a cylindrical cavity by dielectric coating," in *1986 Antennas and Propagation Society International Symposium*, Vol. 24, 305–308, Philadelphia, PA, USA, Jun. 1986.

[7] Yang, S. N., Z. X. Zhang, W. R. Shao, and H. W. Deng, "Numerical investigation on electromagnetic scattering characteristics for engine cavity with centrocone," *Aeroengine*, Vol. 40, 48–53, 2014.

[8] Gao, X., Q.-Z. Yang, H.-R. Mu, and X. Guo, "Numerical simulation of radar scattering characteristics for 2-D nozzles with different aspect ratios," *Journal of Propulsion Technology*, Vol. 35, No. 6, 735–741, 2014.

[9] Hoseini, M., A. Abdolali, M. Fallah, and M. K. Amir-Hosseini, "A new method for optimizing RCS of the nose of flying objects," *Microwave and Optical Technology Letters*, Vol. 57, No. 6, 1361–1365, 2015.

[10] Deng, X. J., X. M. Li, J. Ma, and T. Lu, "Effect on RCS of central cone angle in aero-engine cavity," *Gas Turbine Experiment and*

Research, Vol. 32, No. 06, 31–35, 2019.

[11] Wang, R., Q. Yang, S. Zhang, and K. Du, "Numerical simulation analysis of infrared radiation and electromagnetic scattering characteristics of different mixers," *Engineering, Physics*, 2022.

[12] Zhang, S., Q. Yang, R. Wang, X. Wang, and H. Yang, "Integrated optimization of aerodynamic and electromagnetic characteristics for nozzle central cone," *Journal of Physics: Conference Series*, Vol. 2235, No. 1, 012039, 2022.

[13] Ling, H., R.-C. Chou, and S.-W. Lee, "Shooting and bouncing rays: Calculating the RCS of an arbitrarily shaped cavity," *IEEE Transactions on Antennas and Propagation*, Vol. 37, No. 2, 194–205, 1989.

[14] Zhang, Z., B. Yuan, J. Niu, and W. Zhu, "A new iterative physical optics method based on MFIE for computing the RCS (radar cross-section) of electrically large cavities," in *2008 Asia-Pacific Microwave Conference*, 1–4, Macau, Dec. 2008.

[15] Wang, J., X. Que, Y. Yang, and J. Hu, "Simulation of distributed active cancellation method for radar cross section reduction," in *2024 International Conference on Microwave and Millimeter Wave Technology (ICMMT)*, Vol. 1, 1–3, Bejing, China, May 2024.

[16] Zhou, Z. Y. and J. Huang, "Joint improvements of radar/infrared stealth for exhaust system of unmanned aircraft based on sorting factor pareto solution," *Scientific Reports*, Vol. 11, No. 1, 8251, 2021.

[17] Wang, B. and Q. Wang, "Effect of boundary-layer bleed system on radar stealth and aerodynamic performances of S-duct caret intake," in *2023 2nd International Symposium on Aerospace Engineering and Systems (ISAES)*, 360–366, Nanjing, China, May 2023.

[18] Xiang, H., Q. Yang, X. Wang, and J. Fan, "Study on the influence of vortex generator on aerodynamic and stealth characteristics of serpentine inlet," in *AIAA AVIATION 2023 Forum*, 4433, Jun. 2023.

[19] Deng, J., K. Zhao, L. Zhou, W. Zhang, B. Shu, J. Huang, and Z. Gao, "Aerodynamic/stealth design of S-duct inlet based on discrete adjoint method," *Applied Mathematics and Mechanics*, Vol. 45, No. 4, 725–746, 2024.

[20] Wang, B. and Q. Wang, "Aerodynamic optimization of double S-duct caret intake by self-adapting non-dominated sorting genetic algorithm," *Physics of Fluids*, Vol. 36, No. 9, 2024.

[21] Zhang, X., Q. Yang, Y. He, X. Wang, and S. Zhang, "Aerodynamic and stealth characteristics analysis for a new type of S-shaped inlet with inner bulge," in *Turbo Expo: Power for Land, Sea, and Air*, Vol. 84058, V001T01A011, 2020.

[22] Antar, Y. M. M. and H. Liu, "Effect of radar-absorbing materials on RCS of partially coated targets," *Microwave and Optical Technology Letters*, Vol. 17, No. 5, 281–284, 1998.

[23] Lu, H. H., S. T. Shang, X. Sun, Q. Wang, H. W. Deng, and F. Li, "Influence of radar absorbing medium coating positions in the integrated afterburner on radar scattering characteristics of aero-engine," *Aeroengine*, Vol. 50, No. 04, 68–74, 2024.

[24] Bae, G.-S. and C. Y. Kim, "Broadband multilayer radar absorbing coating for RCS reduction," *Microwave and Optical Technology Letters*, Vol. 56, No. 8, 1907–1910, 2014.

[25] Weinmann, F. and A. Tzoulis, "Numerical modeling results of radar signatures for large and complex targets," in *2008 IEEE Radar Conference*, 1–6, Rome, Italy, May 2008.

[26] Anastassiu, H. T., J. L. Volakis, D. C. Ross, and D. Andersh, "Electromagnetic scattering from simple jet engine models," *IEEE Transactions on Antennas and Propagation*, Vol. 44, No. 3, 420–421, 1996.

[27] Hurst, M. and R. Mittra, "Scattering center analysis via Prony's method," *IEEE Transactions on Antennas and Propagation*, Vol. 35, No. 8, 986–988, 1987.

[28] Guo, K., H. Yin, and X. Sheng, "Research on scattering center modeling for radar target," *Chinese Journal of Radio Science*, Vol. 35, No. 1, 106–115, 2020.

[29] Jia, G. W., P. Yin, S. Shao, and Y. F. Lu, "Radar imaging diagnosis and analysis of typical structure on aircraft," *Chinese Journal of Radio Science*, Vol. 39, No. 3, 442–454, 2024.

[30] Chung, S. S. and S. Tuan, "C261: Electric field distribution inside s-shape air inlet for fighter engine," in *Altair Technology Conference 2021*, China, Virtua, Aug. 2021.

[31] Chia, T.-T., R. J. Burkholder, and R. Lee, "The application of FDTD in hybrid methods for cavity scattering analysis," *IEEE Transactions on Antennas and Propagation*, Vol. 43, No. 10, 1082–1090, 1995.